Case Studies in Thermal Engineering 45 (2023) 102970

Contents lists available at ScienceDirect

Case Studies in Thermal Engineering

journal homepage: www.elsevier.com/locate/csite

Proposing empirical correlations and optimization of **Nu** and $\mathbf{S_{gen}}$ of nanofluids in channels and predicting them using artificial neural network

Atef El Jery [a,b], Andrés Alexis Ramírez-Coronel [c,d], Juan Carlos Orosco Gavilán [e], Nadhir Al-Ansari [f,*], Saad Sh Sammen [g]

[a] Department of Chemical Engineering, College of Engineering, King Khalid University, Abha, 61421, Saudi Arabia
[b] National Engineering School of Gabes, Gabes University, Ibn El Khattab Street, Zrig Gabes, 6029, Gabes, Tunisia
[c] Azogues Campus Nursing Career, Health and Behavior Research Group (HBR), Psychometry and Ethology Laboratory, Catholic University of Cuenca, Ecuador
[d] Epidemiology and Biostatistics Research Group, CES University, Colombia
[e] Universidad Privada Del Norte. Lima, Peru
[f] Civil, Environmental and Natural Resources Engineering, Lulea University of Technology, 971 87, Lulea, Sweden
[g] Department of Civil Engineering, College of Engineering, University of Diyala, Diyala Governorate, Iraq

ARTICLE INFO

Keywords:
Entropy generation
Nusselt number
Machine learning
Artificial neural networks
Nanofluid
Heat transfer

ABSTRACT

Getting the best performance from a thermal system requires two fundamental analyses, energy and entropy generation. An ideal mechanism has the highest *Nu* and the lowest entropy S_{gen}. As part of this research, a large dataset of fluid flow via tubes has been collected experimentally. As well as the inclusion of nanoparticles, analyses are included as well. By using deep learning algorithms, the Nusselt number and total entropy generation are predicted. In both models, the mean absolute error was lower than 5%. To determine the most accurate model, hyperparameter tuning is performed. That is adjusting all the settings in the neural network to attain the best results. The results of the predictive models are compared against experimental and benchmark results. The study incorporates a massive optimization strategy to fine-tune the predictive capabilities of the models. Furthermore, the model's predictive abilities are evaluated through the use of the coefficient of determination R^2. For water and nanofluids flowing through circular, square, and rectangular cross-sections, the proposed models can predict *Nu* and S_{gen}. The results showed remarkable agreement with the experimental results. The models showed an MAE of not higher than 1.33%, which is a great achievement. Also, empirical correlations are proposed for both parameters, and double factorial optimization is implemented. The results showed that to achieve the best results, the Re should be higher than 1600, and the nanoparticle concentration should be 3%. A thorough justification of selected cases is presented as well.

1. Introduction

Increasing heat transfer and efficiency in industries has always been the focus of engineers. Fluids such as water, oil, and ethylene

* Corresponding author.
E-mail addresses: ajery@kku.edu.sa (A. El Jery), arc04878@gmail.com (A. Alexis Ramírez-Coronel), juan.orosco@upn.edu.pe (J.C.O. Gavilán), nadhir.alansari@ltu.se (N. Al-Ansari), Saad123engineer@yahoo.com (S. Sh Sammen).

https://doi.org/10.1016/j.csite.2023.102970
Received 13 February 2023; Received in revised form 26 March 2023; Accepted 30 March 2023
Available online 11 April 2023

glycol have an important impact on heating and cooling various processes. One of the biggest downsides of such fluids is their low thermal properties, which hinder heat exchangers from being more efficient. On the other hand, the thermal conductivity of some solids, such as metals, is several hundred times that of common energy-carrying liquids. Therefore, one approach to increase the thermal potential of common fluids is to spread metallic or non-metallic particles in the base fluid. This idea was first expressed by Maxwell [1], but the particles that Maxwell used were large and caused problems such as a very large increase in pressure drop, blockage, and clogging of pipes. With the progress in nanotechnology, Choi [2] proposed the use of nanoparticles for suspension in the fluid, which is called a nanofluid, and did not have the problems that had occurred before. Based on this, nanofluids are defined as common fluids that have suspended particles in nanometer size. The thermal conductivity of nanofluid with alumina nanoparticles in water was investigated in Ref. [3]. The obtained results indicate an increase in thermal conductivity by using a relatively small volume percentage of nanoparticles. The study of increasing heat transfer was also started by Pak and Cho [4]. The almost 30% increase in the heat transfer coefficient of nanofluids made other researchers show interest in this issue. The experimental results confirm that the increase in the concentration of carbon nanotubes is accompanied by an increase in HTC [5]. Many studies have been dedicated to investigating heat transfer [6–9].

Nanofluids are homogeneous compounds made by uniformly distributing a nanoparticle in a base fluid. The used nanoparticles have a diameter of less than 100 nm and can be a metal, metal oxide, or non-metal type. Since the thermal conductivity of the nanoparticles used is far greater than the thermal conductivity of the base fluid, the thermal conductivity of the nanofluid is greater than that of the pure base fluid. The increase in thermal conductivity of the nanofluid depends on various factors such as nanoparticle concentration, temperature, nanoparticle size, type of nanoparticle and base fluid, and pH.

Numerous studies have studied nanofluids [10–14]. In the following, some of the novel research is presented. Sheikholeslami [15] investigated the effect of nanomaterial on phase change materials. He modeled porous foam with Wiremesh packed approach to examine the impact of porosity on freezing. For the solution of the temperature equation with two sources of radiation and phase change, he used the Galerkin method. In another study, Sheikholeslami [16] studied the effects of nanoparticles in a solar system. His paper combined perforated tape with horseshoe-shaped fins and used hybrid nanoparticles to enhance the thermal properties of the operating fluid. As a result of the addition of θ, the convective coefficient reduced to around 12.02%. Approximately 6.43% more mixing of hybrid nanofluid occurred as PR decreased. Thermal performance increased by approximately 0.18% with increasing Q. Sheikholeslami [17] also studied the effects of nanoparticles on energy storage systems. They presented an air conditioning system in their study, and the effects of nanoparticles were studied. As a result of mixing nanoparticles with paraffin, better conduction resulted in a reduction in the required time for full melting by about 5.22% when $Re = 7000$, $\gamma = 0.95$. The time needed for full melting was decreased by 37.15% when $Re = 7000$, $\varphi = 0.035$. The minimum time for full melting in tests was 7985 s, achieved with $\gamma = 0.95$, $\varphi = 0.035$, and $Re = 7000$. In another study, Sheikholeslami and Ebrahimpour [18] used multi-way twisted tape to ameliorate the thermal performance of the Linear Frensel Reflector (LFR) unit. They concluded that as turbulent intensity increases, thermal irreversibility decreases while the friction component increases. They also observed that nanopowders could increase heat output by about 0.153%. In a study by Esfahani and Shahabi [19], the impact of heat fluxes on the wall of a pipe containing a laminar and fully-developed flow was studied, and the entropy generation (S_{gen}) was measured numerically. In this study, the operating fluid Prandtl number is 13400, and the Reynolds number is 0.5. The results of this study show that the highest S_{gen} is in the case of descending heat flux, and there is very little difference in S_{gen} in the cases of constant heat flux and ascending heat flux. A study by Noghrehabadi et al. [20] investigated the S_{gen} of a nanofluid flowing on a tension sheet. In the vicinity of the sheet, heat generation parameters and Brownian motion parameters were increased to reduce S_{gen}. Wang et al. [21] investigated the S_{gen} in a square cavity. With respect to the irreversibility rate in general and the Richardsons number in particular, the Bejan number also decreased. According to Zhou et al. [22], S_{gen} is minimized when optimizing heat exchangers. With a decreasing optimal heat transfer distribution ratio, the lowest S_{gen} occurs. Falahat et al. [23] studied the S_{gen} in a circular channel. By decreasing the power law index and channel length parameters in this study while maintaining a constant Re number, the overall S_{gen} was reduced. With rising wall temperature and nanoparticle concentration, the total S_{gen} both rose and fell. Abdollahi et al. [24] numerically investigated the flow of a nanofluid in a microchannel using porous media. They concluded that a smaller volume of heat is transferred with a slower Nusselt number when hybrid mixtures are added to water. Porosity values and Brownian movement of nanoparticles cause higher thermal conductivity, causing heat to transfer to the environment. Jalili et al. [25,26] investigated a micro-polar nanofluid in a rotating system. They have shown that it is very effective and practical for solving these types of coupled equations. The obtained results show a 6% difference between the obtained values and the previous ones. Jalili et al. [26] also used a magnetic field to investigate a cylindrical polar system. They proposed a novel approach to solve the governing equations, and the results were promising. In another study [27], they performed a semi-analytical method to solve Williamson nanofluid flow. The results using the Akbari-Ganji method proved to be more accurate than their previous studies. They also investigated the results of adding nanoparticles in various cases [28–32].

One of the very important variables in equipment that uses nanofluid flow for heat transfer is the HTC of nanofluid. Since both the amount of thermal conductivity and convective heat transfer is effective in the flow temperature distribution, the changes in the *Nu*, which is the dimensionless ratio of these two values, are investigated in the articles. In recent years, many studies have been conducted on convective heat transfer in laminar flow [33,34] and turbulent flow [35–38].

Some researchers have also studied the mathematical modeling of nanofluid convective heat transfer [39]. Some of them have considered the nanofluid as a single phase. They have considered an average of the physical properties of the nanoparticle and the base fluid as the properties of the nanofluid [40,41], and another group of researchers has modeled the nanofluid as a two-phase flow [42,43]. Since, in industrial applications, the fluid or nanofluid used for heat transfer is usually modeled as a laminar flow in tubes of various cross-sections, several articles have investigated this flow type. For example, Mansour [44], Nambro [45], and Maiga [46]

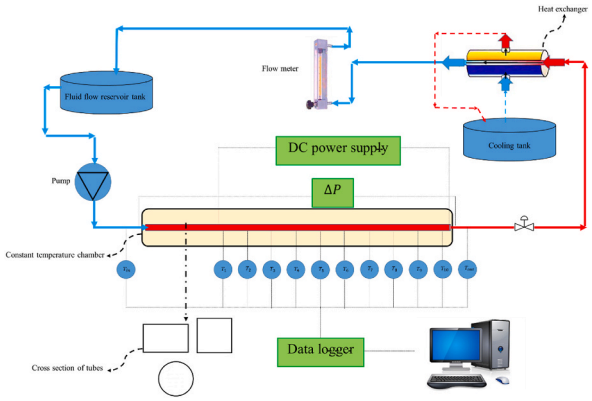

Fig. 1. The experimental setup of [52].

Table 1
The properties of different cases.

Cross section	2a	2b	2b/2a	Dh
Square	0.0154	0.0154	1	0.0154
Rectangular	0.0231	0.01155	0.5	0.0154

modeled the turbulent flow inside a circular tube by assuming that the nanofluid is single-phase, and Behzadmehr [47] considered the nanofluid as two-phase and modeled it.

In abundant studies, artificial intelligence is widely used to optimize and predict objective functions. An alternative method for studying and proposing models on these phenomena is deep learning methods such as artificial neural networks (ANN). This method, which has been widely used to model nanofluid properties [48,49], models existing experimental data by combining complex mathematical relationships and can predict the behavior of the problem in new conditions. Some examples of such models are presented in the following.

Alimoradi et al. [50] investigated subcooled flow boiling of nanofluid in a tube with a circular cross-section and simulated it numerically. Deep learning models with surprising results were presented using simulation data. Heat transfer and bubble dynamics were investigated in the boiling process. Also, the model showed the ability to extrapolate. Alimoradi and Shams [51] investigated subcooled flow boiling and presented an optimization model using the genetic algorithm to study the critical heat flux. They examined the most optimal mode in terms of heat transfer.

This research aims to use the results of [52] on the convective heat transfer of fluid flow inside a tube with various cross-sections. Using the experimental data, predictive models are proposed for predicting *Nu* and S_{gen}. The mentioned output parameters are predicted locally and on average. We have utilized hyperparameter tuning to look for the best predictive models. Finally, the artificial neural network models' predictive capabilities are evaluated, and the data's clear visualization is presented. In the present study, a novel method of results prediction based on machine learning algorithms is applied to the experimental results of our previous study [52]. In order to carry out the procedure, a method called hyperparameter tuning is applied. In this method, we use a single factorial optimization process to adjust the key parameters in the predicting algorithm. This way, we were able to achieve predictive models with very low errors and high predictive capabilities. Finally, a double factorial optimization method is utilized, and correlations for the studied parameters are proposed.

2. Experimental setup and its components

2.1. Experimental setup

In the present study, we have utilized the experimental results obtained from our previous research, and all the methodology and governing equations are presented in Ref. [52]. The results are completely validated, and the variety of data helps build inclusive models for different flow patterns in various cross-sections. Fig. 1 presents the experimental setup of our previous study [52]. The properties of these cases are given in Table 1, and the hydraulic diameters of all cases are identical.

The analyses of the experimental data and whether the results are valid are thoroughly discussed in Ref. [52]. In the present study, the mentioned results are gathered to propose new models using artificial neural networks (ANNs). The codes for this model are written in Python. The procedure carried out on the data is presented in the following. A complete uncertainty analysis is presented in our previous research [52], and the uncertainty is not more than 2%.

3. Artificial neural networks

The multilayer perceptron (MLP) network is a shared and widely used network for neural network design [53] in this research. In

MLP networks, each neuron is connected with several other neurons in its neighborhood, and by changing the weight coefficients, the influence of each input neuron is adjusted relative to other input neurons. After the inputs are multiplied by the resulting weight coefficients, they are added together, and the result is transferred to the neurons of the next hidden layer employing an activation function. This work continues until the last layer, which is the network's output [54].

$$\gamma_{ij} = F_k\left(\sum_{i=1}^{N_{k-1}} w_{ij}\gamma_{i(k-1)} + \beta_{jk}\right) \tag{1}$$

In equation (1), γ is the value of neurons, k shows the number of layers, w is the weight coefficients, β is the bias value, and F represents the activation function. After being multiplied by the weight coefficients and added with the bias value, the values of the neurons of the previous layer are added together and placed in the activation function to obtain the value of the neuron of the next layer. The user selects the activation function, and the values of the weighting coefficients are determined in the training phase of the neural network by trial and error in such a way that the output of the neural network has the least error compared to the outputs obtained from the experimental data.

In this modeling, 67 experimental data were extracted by experimenting on flow through tubes of different cross-sections. The number of local data is 667. Python is used to construct the ANN models in the present study. In this modeling, 70% of this data was used for training and 30% for testing. To construct the ANN model, a hyperparameter tuning process is done. In this procedure, all the user-defined functions of the ANN model are investigated, and the best model is finally selected for the output parameter.

In order to get the best results from the ANN models, all the contributing factors have to be adjusted. This process is called hyperparameter tuning. In the following, all the contributing factors have been refined to identify the optimum model [55]. It should be emphasized that building the widest and deepest network possible may not always be the best option. On the other side, the model would encounter the overfitting issue if the hidden layers were increased excessively.

The improved ANN's hyperparameters employed in the current investigation are as follows. The rate of learning is set at 0.001. Naturally, greater values might be selected to reach convergence more quickly, but this could also result in disruption close to the optimal point. The gradient descent solution in this investigation is the Adam optimizer [56].

The loss function of the present models is the MSE. This function is responsible for updating the weights and biases in the back-propagation process. The MSE is calculated as follows:

$$E_m = \frac{1}{n}\sum_{i=1}^{n}(Y_i - \widehat{Y}_i)^2 \tag{2}$$

When the training process is carried out, the models require to be evaluated. In the present study two parameters are chosen for this. The first is the MAE. The MAE is formulated as:

$$\mathrm{MAE} = \frac{1}{n}\sum_{i=1}^{n}\frac{|Y_i - \widehat{Y}_i|}{Y_i} \times 100\% \tag{3}$$

In Equations (2) and (3), n is the number of cases, Y_i is the experimental value, and $\widehat{Y}_i$ is the predicted value of the model.

The second metric for the evaluation is the R-squared or R^2. This parameter shows the capability of the predictive model to predict the output parameter. R^2 is formulated as:

$$R^2 = 1 - \frac{\sum(Y_i - \widehat{Y}_i)^2}{\sum(Y_i - \overline{Y})} \tag{4}$$

In equation (4), $\overline{Y}$ is the mean of the data.

4. Results and discussion

The experimental results are later compared with the ANN model predictions, and more discussion is devoted to the results. However, deep learning-based predictive models are proposed to avoid further experiments. Interestingly, the results of the predictive models are so accurate that it seems like this is the logical path to save more time and resources.

4.1. Artificial neural networks

The desired parameters are predicted using a synthetic neural network. As was already indicated, the best model has to be tuned, and it is a time-consuming process which needs to be conducted with great care. Thus, for each objective function, we do a hyper-parameters tuning process. The process connected with the local *Nu* for circular cross-section is illustrated in the next section. The exact process is used in this investigation for all goal quantities.

Finding out how many hidden layers there are is the first step. The number of hidden layers is determined using the famous doubling sequence, starting with 32 neurons. Since neurons and hidden layers are the main parts of the neural network, it is necessary to look at their numbers at the beginning of the procedure. Table 2 indicates the study of the number of neurons and the structure of hidden layers on the final predictive capabilities of the models.

Based on Table 2, the number of hidden layers plays a considerable role in the predictive results. In other words, the accuracy

Table 2
Different structures for hidden layers (HL).

Model	Inlet	HL	MAE	R^2
1	$x/D, Re, A_c, \varphi$	(32)	2.42%	0.95
2		(32,64)	2.09%	0.96
3		(32,64,32)	1.98%	0.96
4		(32,64,64,32)	1.73%	0.97
5		(32,64,128,64,32)	1.68%	0.97
6*		(32,64,128,128,64,32)	1.45%	0.98
7		(32,64,128,256,128,64,32)	1.56%	0.97
8		(32,64,128,256,256,128,64,32)	1.48%	0.97
9		(32,64,128,256,512,256,128,64,32)	1.52%	0.97

* Selected model.

Table 3
Investigation of activation function of output layer.

Model	HL	Output Activation Function	MAE	R^2
1	(32,64,128,128,64,32)	Linear	1.51%	0.97
2*		ReLU	1.41%	0.98
3		Sigmoid	1.87%	0.96

* Selected model.

Table 4
Investigation of batch size.

Model	HL	Batch size	MAE	R^2
1	(32,64,128,128,64,32)	2	1.89%	0.96
2		4	1.61%	0.96
3		8	1.52%	0.97
4		16	1.40%	0.98
5[a]		32	1.39%	0.98
6		64	1.45%	0.97

[a] Selected model.

Table 5
Investigation of epochs.

Model	HL	Epochs	MAE	R^2
1	(32,64,128,128,64,32)	1000	2.58%	0.95
2		2000	2.42%	0.95
3		5000	1.94%	0.96
4		10,000	1.68%	0.97
5[a]		20,000	1.37%	0.98
6		30,000	1.39%	0.98
7		40,000	1.40%	0.98
8		50,000	1.39%	0.98

[a] Selected model.

increases as the number of layers augments, but this increase is up until the overfitting. When this problem happens, the accuracy drops considerably, and the model loses its potential to generalize its predictive results. This is because the model trains exclusively for the training dataset in overfitting, but it loses its ability to capture data points other than the training dataset. Therefore, the best model is selected in Table 2. The next parameter that needs careful attention is the activation functions in the output layer. The results are presented in Table 3.

The number of data points in every feed-forward process is called batch size. This parameter is also effective in the results of the models. Therefore, the batch size is investigated in Table 4. It is observed that overfitting occurs in this parameter. By decreasing the batch size, the model is more likely to overfit. By comparing the results, 32 is the best case.

Also, the number of iterations for adjusting the weights and biases, i.e., epochs, is presented in Table 5. The best model is chosen based on the epochs. The results show that the increase in epochs does not necessarily improve the predictions, so this parameter must be selected to achieve the best result.

As was mentioned, it is important to adjust the hyperparameters in the ANN model, and the results are highly dependent on how

Table 6
The settings for final models.

Objective function	Cross-section	Inputs	Hidden layers	Epochs	Batch size	Activation Function
Nusselt average	Circular	Re, A_c, φ	(32,64,128,64,32)	40,000	32	ReLU
Nusselt average	Square	Re, A_c, φ	(128,64,32)	30,000	8	ReLU
Nusselt average	Rectangular	Re, A_c, φ	(512,256,128,64,32)	30,000	16	ReLU
Nusselt local	Circular	$x/D, Re, A_c, \varphi$	(32,64,128,128,64,32)	20,000	32	ReLU
Nusselt local	Square	$x/D, Re, A_c, \varphi$	(128,128,64,64,32,32)	10,000	8	Linear
Nusselt local	Rectangular	$x/D, Re, A_c, \varphi$	(32,64,128,64,32)	20,000	4	ReLU
$S_{gen.ave}$	Circular	Re, A_c, φ	(32,64,32)	10,000	16	ReLU
$S_{gen.ave}$	Square	Re, A_c, φ	(64,64,32,32)	10,000	32	Linear
$S_{gen.ave}$	Rectangular	Re, A_c, φ	(256,128,64,32)	8000	64	ReLU
$S_{gen.loc}$	Circular	$x/D, Re, A_c, \varphi$	(128,128,64,64,32,32)	40,000	32	ReLU
$S_{gen.loc}$	Square	$x/D, Re, A_c, \varphi$	(512,256,128,64,32)	10,000	64	Sigmoid
$S_{gen.loc}$	Rectangular	$x/D, Re, A_c, \varphi$	(128,64,32)	30,000	16	ReLU
Nusselt average	All	Re, A_c, φ	(32,64,128,64,32)	20,000	16	Linear
Nusselt local	All	$x/D, Re, A_c, \varphi$	(32,64,128,256,256,128,64,32)	40,000	32	ReLU
$S_{gen.ave}$	All	Re, A_c, φ	(256,256,128,128,64,64,32,32)	30,000	16	ReLU
$S_{gen.loc}$	All	$x/D, Re, A_c, \varphi$	(256,256,128,128,64,64,32,32)	50,000	8	Sigmoid

well these parameters are set. The mentioned procedure proved that the importance of hyperparameter tuning could be significant. The best results are attained by carrying out this process for all the output parameters, which are presented in Table 6.

4.2. Model evaluation and performance

We have selected Re, A_c, φ and $x/D, Re, A_c, \varphi$ for the average and local input parameters. These parameters are able to predict the output parameter because they have all the physical definitions of the flow. Therefore, the models have high accuracies. When the training process ends, we have to evaluate the models using unseen data points. Consequently, the testing data points are utilized for this purpose. The data predictions are visualized and compared with the best case in the following sections.

4.2.1. Nu for circular cross-section

The average and local *Nu* of the circular cross-sections are presented in Fig. 2a and b. For the average *Nu*, 20 data points are employed for evaluating the predictive model. However, in the local *Nu*, 200 testing data points are utilized. Fig. 2a shows the predicted average *Nu* of circular cross-sections against the experimental results. The MAE of this model is 2.42%. Also, this model was able to attain an R_squared of 0.96. The hidden layers' structure is 32,64,128,64,32. The local *Nu* dataset has 200 testing data points. Fig. 2b indicates the model prediction of the local *Nu* for circular cross-sections. It is clear that the model was able to accurately model the flow, so both metrics are favorable. Also, the results of the local case are more accurate than the average ones. As seen in Fig. 2, the blue line is the ideal case (y = x), and two parallel lines of 10% errors are drawn to help better visualize the results and their deviation from the ideal case.

4.2.2. Nu for square channels

The square channel is the following case for the predictive models. The average and local *Nu* of this geometry is indicated in Fig. 2c and d. Similar to the circular case, the number of data points on which the proposed models are tested is 20 on average and 200 for local cases. The ANN model is structured in a 128,64,32 pattern. The results of the proposed model for the average *Nu* are an MAE of 2.03% and an R^2 of 0.97. The local *Nu* presented in Fig. 2d indicates the model prediction for square cross-sections. The results of the proposed model demonstrate that it is able to get the MAE of 1.25% and the R^2 of 0.99.

4.2.3. Nu for rectangular channels

The rectangular cross-section is also investigated in the present study. The proposed models for average and local *Nu* are illustrated. Fig. 2e shows the proposed model's result for the average *Nu* of rectangular cross-sections. The model is evaluated with 20 data points. The model's accuracy in prediction is measured by MAE and R^2 which are 1.39% and 0.98, respectively. The local *Nu* is tested on 200 data points. Fig. 2f shows the results of the proposed model for this parameter. It is observed that the accuracy of this model is more than the circular case. The deviations from the ideal case are less than the circular one. The MAE of this model is 1.46%, and the R^2 is 0.98. This shows the high capabilities of the proposed models. The hidden layer structure of the proposed model is 32,64,64,32.

4.2.4. S_{gen} for circular tubes

Similar to the *Nu*, the S_{gen} of the present study is investigated locally and on average. The results of the average S_{gen} are presented in Fig. 3a. It is observed that the proposed model for the average S_{gen} has an MAE of 1.29%, and its R^2 is 0.98. Also, the ANN model structure is as simple as 32,64,32. Thus, the runtime of the model is extremely low. However, the local S_{gen} model utilizes a more complicated ANN model structure based on Fig. 3b. Therefore, the runtime is three times the average model. This is also because the number of training data points varies in both models. The local model is trained on 467 data points and tested on 200 data points. However, the average case is trained on 47 data points and evaluated on 20 data points. The model for local S_{gen} in circular cross-section achieved the MAE of 3.67% and R^2 of 0.94. Given the variety of cases studied in the present work, it is acceptable to achieve such accuracies.

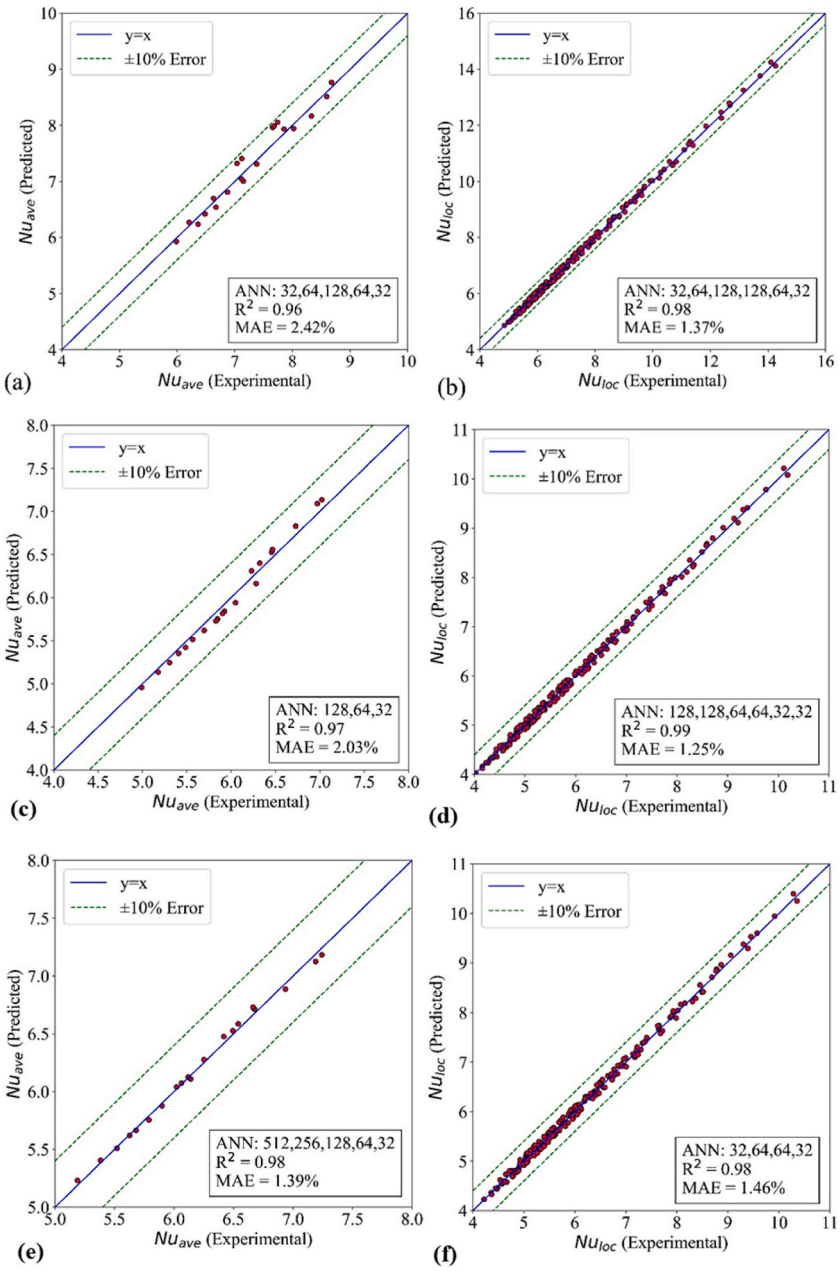

Fig. 2. The ANN models of for (a) circular cross-sections average *Nu*, (b) circular cross-sections local *Nu*, (c) square cross-sections average *Nu*, (d) square cross-sections local *Nu*, (e) rectangular cross-sections average *Nu*, and (f) rectangular cross-sections local *Nu*..

4.2.5. S_{gen} for square channels

The average case shown in Fig. 3c has the ANN model of 64,64,32,32. The model for the average S_{gen} was able to achieve the MAE of 2.19% and R^2 of 0.96. The results of this case show a good agreement with the ideal case (y = x), which is the experimental data. The predictions for local S_{gen} in square cross-section are presented in Fig. 3d. It is concluded that the MAE increases to 3.98% in the local case. This shows that the predictive capabilities of this model are lower than the average case. Also, the R^2 of the proposed model is equal to 0.93. Notably, the ANN model structure of the proposed model is more complicated than the average case with the following pattern 512,256,128,64,32.

4.2.6. S_{gen} for rectangular channels

Fig. 3e–f presents the results of S_{gen} for rectangular cross-sections. The average S_{gen} in this geometry is evaluated using 20 testing data points. The metrics used for measuring this parameter show that the MAE is 1.57%, and the R^2 is equal to 0.97. The model is mounted on an ANN structure of 256,128,64,32. The results of this parameter have good agreement with the experimental results. The

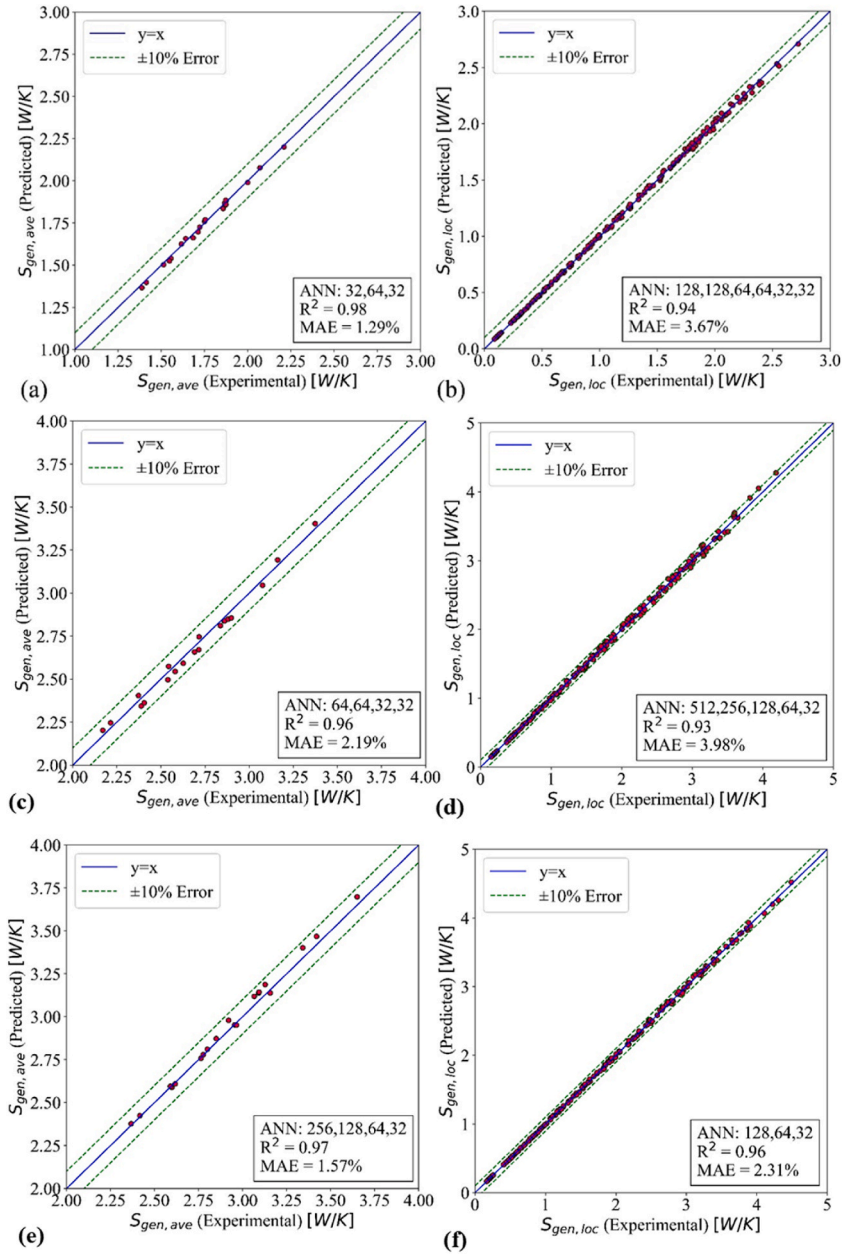

Fig. 3. The ANN models of for (a) circular cross-sections average S_{gen}, (b) circular cross-sections local S_{gen}, (c) square cross-sections average S_{gen}, (d) square cross-sections local S_{gen}, (e) rectangular cross-sections average S_{gen} and (f) rectangular cross-sections local S_{gen}.

predictions of local S_{gen} are presented in Fig. 3f. This model is tested with 200 testing data points. The MAE of this model is 2.31%, and the R^2 of this model 0.96. Compared to other cross-sections, the predictive results of the S_{gen} in rectangular tubes are more accurate. Interestingly, the ANN model of this objective function is so simple (128,64,32). This is the logic behind the hyperparameter tuning. The more complicated models do not necessarily present better results.

4.2.7. The final models for Nu

Finally, to propose an applicable model for all cross-sections in all the mentioned cases, we present our models for both average and local *Nu* in Fig. 4. The overall models trained on the whole dataset show great results regardless of their cross-sections. The model for the average *Nu* shown in Fig. 4a shows that it has achieved the MAE of 2.98%. This is a little more than the others, but it should be noted that this model is accumulating the datasets; as a result, it is natural to observe a little increase in the MAE. The R^2 of this model is 0.95, which is very good in terms of prediction. The local *Nu* predictions are shown in Fig. 4b, and it has the ANN structure of 32,64,128,256,256,128,64,32. As can be seen, this is the most complicated ANN structure in the present study. The reason for this is

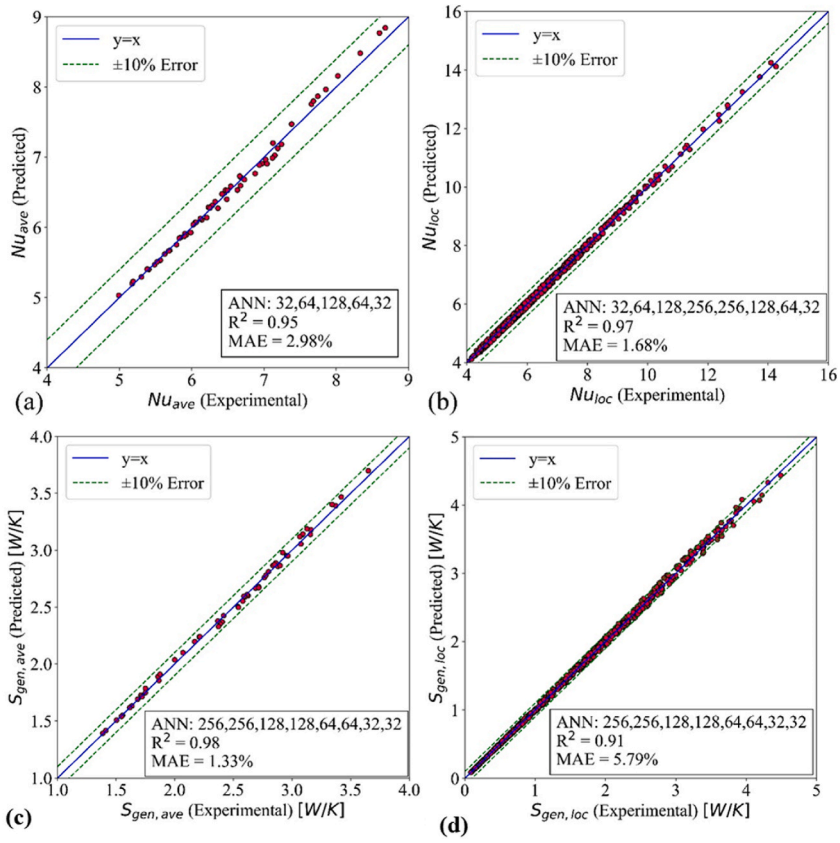

Fig. 4. The ANN models capabilities evaluated on all datasets for (a) average *Nu*, (b) local *Nu*, (c) average S_{gen}, and (d) local S_{gen}.

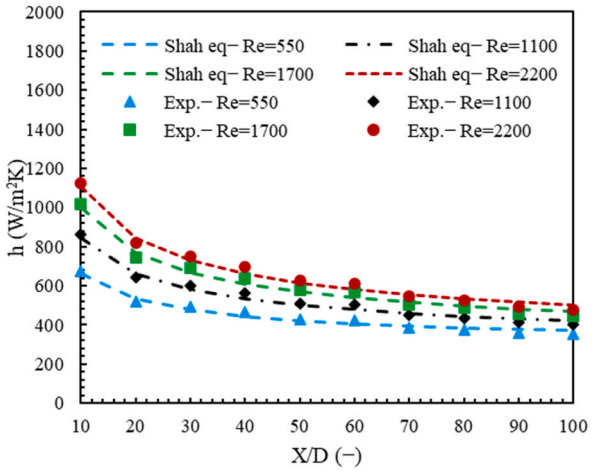

Fig. 5. The validation case of the present study [52].

the complicated interactions between the datasets, and to fully understand these connections, a more complicated ANN model is required. The run time of this model is far higher than the other counterparts. This model has achieved the MAE and R^2 of 1.68% and 0.97, respectively.

4.2.8. *The final models for S_{gen}*

Like the *Nu*, the S_{gen} of all cross sections is considered in one model. This model proposes a predictive ANN that applies to all cross-sections studied in the present work. These overall models' accuracy is relatively lower than the exclusive ones, but these are more applicable in industries. Fig. 4c shows predictive results of the total average S_{gen}. This model is trained on 141 data points and

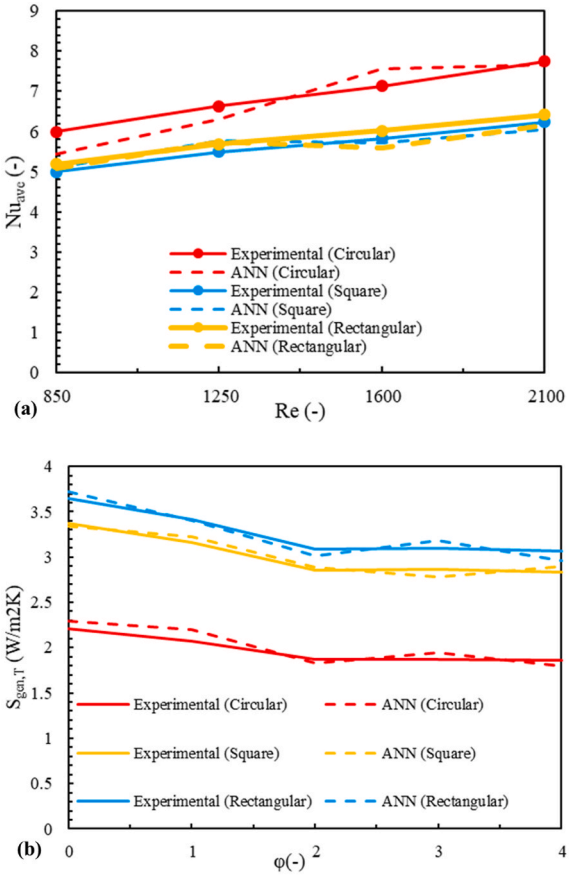

Fig. 6. Comparative study of (a) average *Nu* and (b) average S_{gen} ANN results vs. the experimental results.

evaluated with 60 testing data points. The results of the mentioned model show that the MAE is 1.33%, and the R^2 is equal to 0.98. Surprisingly, the proposed model has outstanding accuracy in predicting S_{gen}. This would help avoid time-consuming experiments. The ANN model structure is 256,256,128,128,64,64,32,23. The model for local S_{gen} is shown in Fig. 4d. The proposed model was able to achieve the MAE of 5.79% and the R^2 is 0.91. Clearly, the model is able to predict the local S_{gen} with great accuracy, so this could be applicable in the designing process of a thermal system. The model's structure is also 256,256,128,128,64,64,32,32. In Fig. 4d, the predictions are so close to the experimental results, so the points are in the vicinity of the ideal case.

4.3. Model visualization vs. experimental data

Before the results are compared, the validation of the present results against the benchmark Shah-London results is presented. The results in Fig. 5 show that the results of the present study have good agreement with the benchmark results [52].

The visualization of the extracted results from the experiments is presented in the following to analyze the data in the current research. The influence of Re number and nanoparticle addition are investigated, and the optimum point in increasing the Re number and nanoparticles in the base fluid is studied. Finally, a comparative study of the unseen experimental data and the predictive models is carried out, which clearly determines the proposed models' predictive capabilities. The predictive ANN model for the average *Nu* is presented here to predict unseen data in different cases. It is shown that the overall model results can capture the problem's cross-section, and it has achieved phenomenal results. Fig. 6a shows the comparative results of the experimental data and the predictive results of the overall ANN model for the average *Nu*. It is clear that although there might be some minor differences between the experimental and the predictive results, the models can capture the trend on which the average *Nu* is changing. Moreover, the average S_{gen} is studied similarly to the *Nu*, and the results of the S_{gen} are in concordance with the analytical results. Fig. 6b shows S_{gen} in various geometry and their predictions.

4.4. Empirical correlations and optimization

In this section, high-accuracy empirical correlations for Nusselt number and entropy generation for various cross sections. These models are based on Reynolds number and nanoparticle concentration. The general polynomial equation of the models is presented as equation (5).

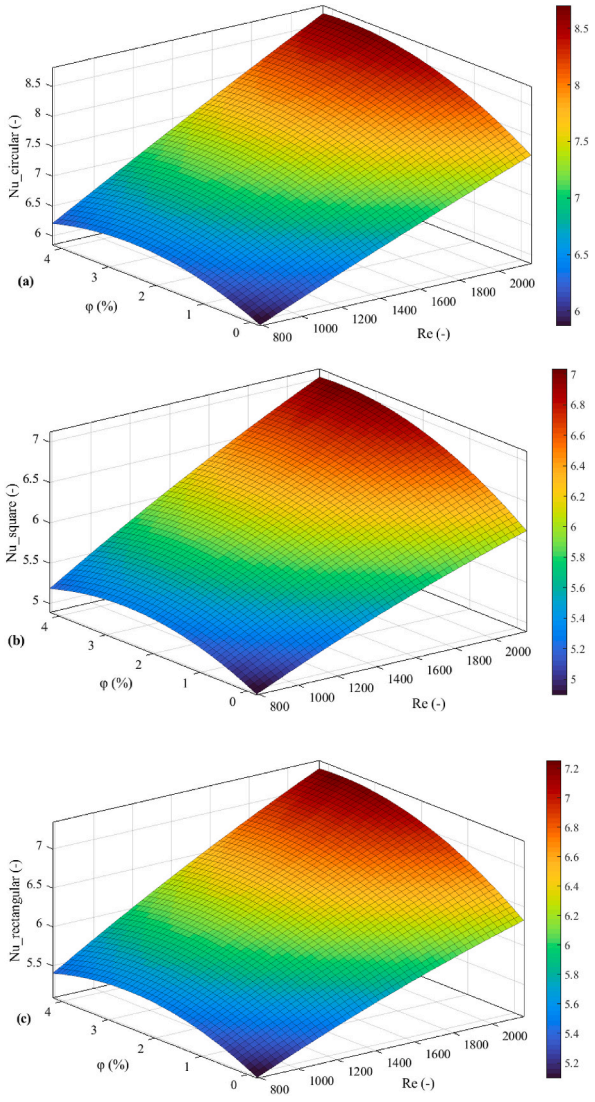

Fig. 7. Average *Nu* of (a) circular, (b) square, and (c) rectangular cross-sections.

Table 7
The constant values for Nu_{ave} for different Re and φ and the evaluation of the correlations using RSME and R^2.

Cross-section	A_1	A_2	A_3	A_4	A_5	A_6	RMSE	R^2
Circular	4.791	0.001509	0.2683	−6.121e-08	0.0001119	−0.06984	0.09	0.99
Square	3.993	0.001337	0.2173	−1.406e-07	9.886e-05	−0.05755	0.07	0.98
Rectangular	4.207	0.001319	0.2275	−1.378e-07	0.0001016	−0.05956	0.07	0.98

$$Output = A_1 + A_2x + A_3y + A_4x^2 + A_5xy + A_6y^2 \quad (5)$$

4.4.1. Nusselt number

The optimized values of Nu_{ave} in different cross sections are presented in Fig. 7 based on the correlation of equation (5) and coefficients of Table 7.

As can be seen in Fig. 7a, in order to achieve the highest NU_{ave} in circular tubes, Re should be higher than 1800, and nanoparticle concentrations higher than 3%. It should be noted that the correlation in equation (5) is based on dimensionless numbers, and it is easy to implement. A similar trend is observed for square channels, and the highest average *Nu* is achieved in the Re of higher than 1850. It should be noted that the amount of 3% and 4% nanoparticle concentration does not significantly affect the *Nu*, so it is logical to select the nanofluid with 3% concentration because it is more stable.

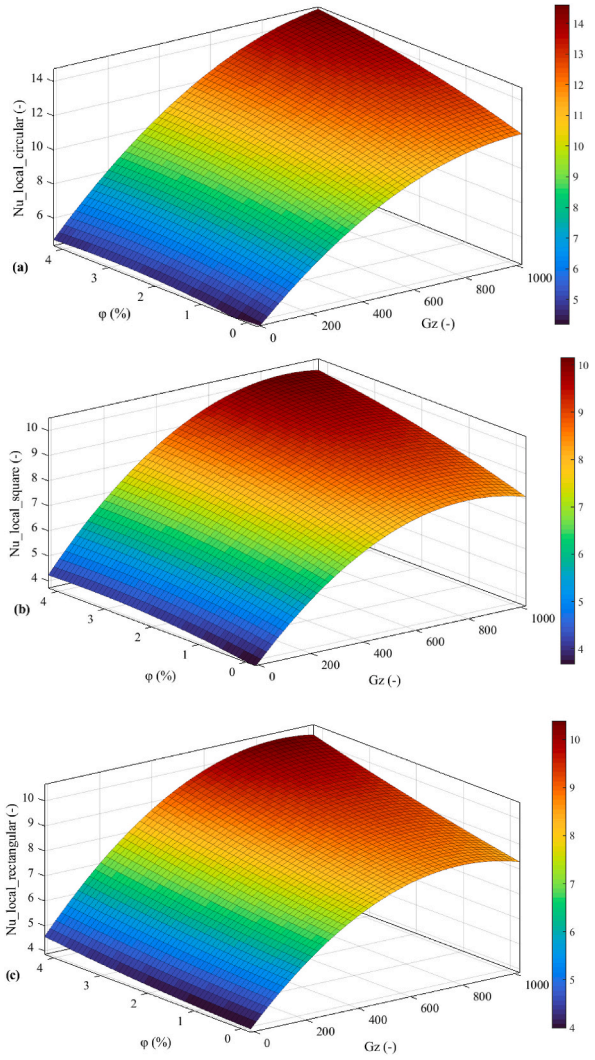

Fig. 8. Local *Nu* of (a) circular, (b) square, and (c) rectangular cross-sections.

Table 8
The constant values for Nu_{loc} for different Gz and φ and the evaluation of the correlations using RSME and R^2.

Cross-section	A_1	A_2	A_3	A_4	A_5	A_6	RMSE	R^2
Circular	4.445	0.01501	0.4001	−7.261e-06	0.0004499	−0.06804	0.23	0.98
Square	3.876	0.0117	0.3054	−7.305e-06	0.0003069	−0.04376	0.23	0.97
Rectangular	4.135	0.01154	0.05513	−7.256e-06	0.0003062	0.02029	0.27	0.95

A similar analysis is presented for Nu_{loc} in Fig. 8. The coefficients of equation (5) for Nu_{loc} are presented in Table 8. The x and y, for this case, are Graetz number and nanoparticle concentration.

For Nu_{loc}, we are also looking for the maximum value, so the places with the highest *Nu* is considered. For circular tubes, as in Fig. 8a, the highest Nu_{loc} is observed from Gz of 800–1000. The best nanoparticle concentration for this case is from 3% to 4%. As presented in Fig. 8b, the optimum ranges for square channels are in GZ of 600–1000 and nanoparticle concentration of 3%–4%. In Fig. 8c, the figure for Nu_{loc} of the rectangular channel is presented. In this case, the highest *Nu* is from Gz of 600–1000 and nanoparticle concentrations of 3% and 4%. These results reiterate the mentioned points about nanoparticle concentration. In other words, as the concentration increase, the *Nu* enhances.

4.4.2. Entropy generation

The empirical correlations for S_{gen} are also proposed, and the optimum points are determined. As was mentioned earlier, equation (5) is used for all cases, but the correlations of each case differ. The coefficients of equation (5) for $S_{gen_{ave}}$ are presented in Table 9.

Table 9
The constant values for $S_{gen_{ave}}$ for different Re and φ and the evaluation of the correlations using RSME andR^2.

Cross-section	A_1	A_2	A_3	A_4	A_5	A_6	RMSE	R^2
Circular	2.662	−0.0006345	−0.1688	9.267e-08	8.615e-07	0.02064	0.02	0.99
Square	4.029	−0.0009397	−0.2509	1.556e-07	−5.871e-06	0.0313	0.03	0.99
Rectangular	4.324	−0.0009647	−0.2722	1.578e-07	−7.312e-06	0.03401	0.04	0.99

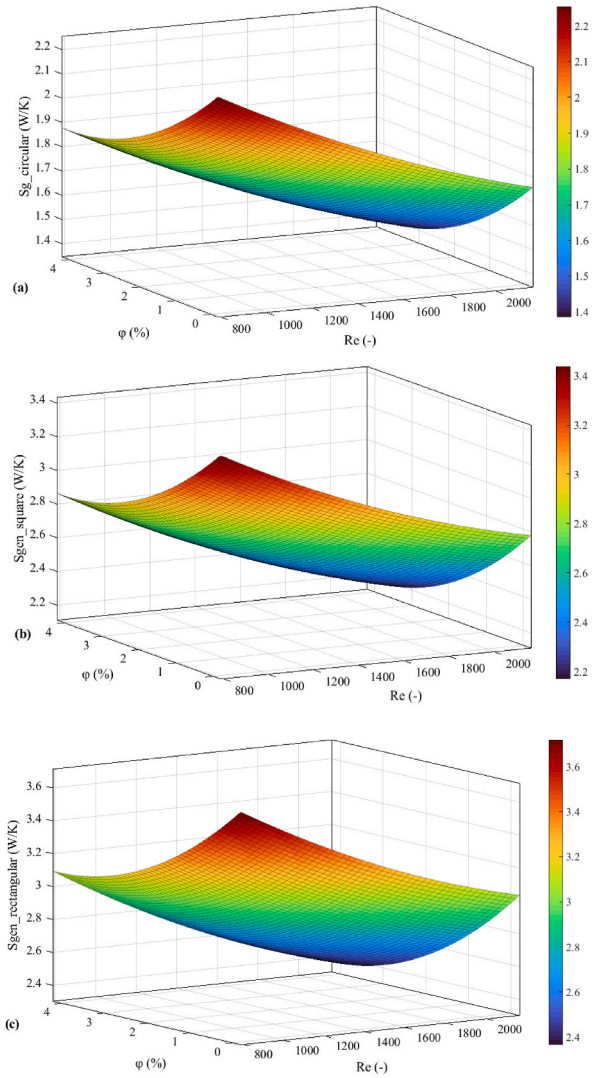

Fig. 9. The average S_{gen} of (a) circular, (b) square, and (c) rectangular cross-sections.

Table 10
The constant values for $S_{gen_{loc}}$ for different Gz and φ and the evaluation of the correlations using RSME andR^2.

Cross-section	A_1	A_2	A_3	A_4	A_5	A_6	A_7	RMSE	R^2
Circular	2.9	−0.01635	−0.1363	3.01e-05	0.000505	−1.691e-08	−5.127e-07	0.30	0.82
Square	4.375	−0.02466	−0.2124	4.57e-05	0.000784	−2.572e-08	−7.967e-07	0.45	0.81
Rectangular	4.785	−0.02691	−0.2321	4.98e-05	0.000863	−2.801e-08	−8.771e-07	0.49	0.81

In contrast to the Nusselt, the entropy generation should be minimized to achieve the best result, so in Fig. 9, we looked for the minimums. As can be seen in Fig. 9a, the entropy generation for circular tubes is minimized when Re is from 1600 to 2000, and the nanoparticle concentration is more than 2%. The best case is achieved when nanoparticle concentration is 3%. The entropy generation

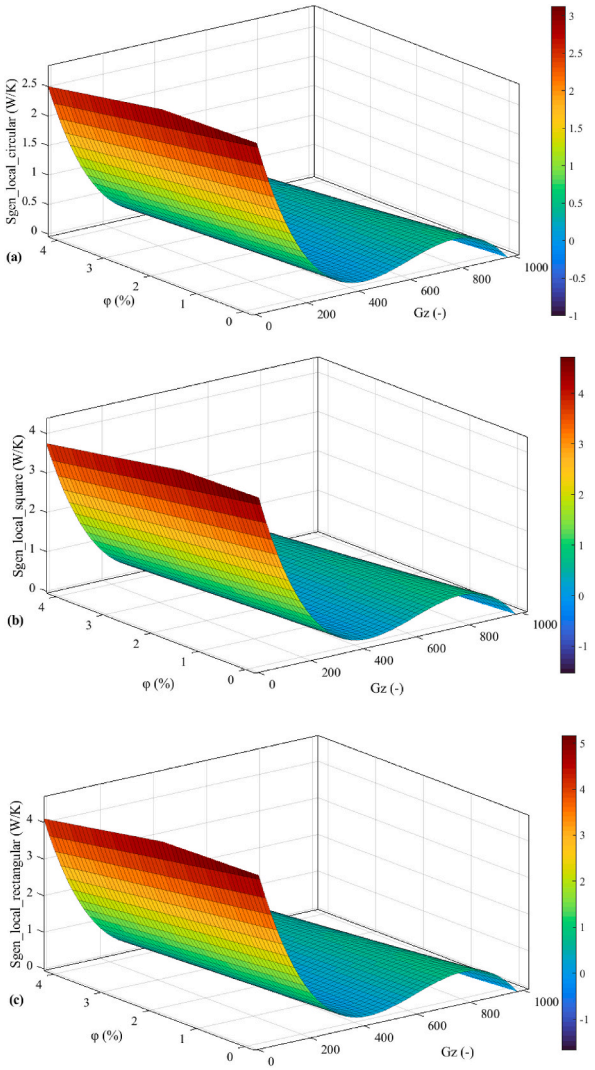

Fig. 10. The local S_{gen} of (a) circular, (b) square, and (c) rectangular cross-sections.

of the square channel follows a similar trend with one difference that the value of S_{gen} is higher for this cross-section, as seen in Fig. 9b. The optimum values for square channels are the same as those of circular ones. Fig. 9c presents the S_{gen} values for rectangular channels. The optimum case for this cross-section is observed when nanoparticle concentration equals 3%, and the *Re* is from 1500 to 2000.

The correlation for the local entropy generation differs from the others and is presented in equation (6). The alternative equation presents the trends more accurately than equation (5). The coefficients for this parameter are presented in Table 10.

$$S_{gen_{loc}} = A_1 + A_2x + A_3y + A_4x^2 + A_5xy + A_6x^3 + A_7x^2y \tag{6}$$

The minimum of local entropy generation is observed in Gz number higher than 900, and the nanoparticle concentration does not affect the entropy generation significantly, as seen in Fig. 10a. The local entropy generation for square channels is presented in Fig. 10b, and it shows the significance of Gz number on the entropy generation. Also, Fig. 10c depicts the results for rectangular channels. The results of square and rectangular channels are similar to circular tubes, and in the mentioned range, the entropy is minimized.

5. Conclusions

The experimental results of our previous study [52] have been used to provide predictive models for various parameters. Moreover, the S_{gen} of the flow is calculated using analytical relations. The results of water are then compared to nanofluids with various concentrations. To further increase the applicability of the previous study, the gathered results are used to create ANN models to predict the output parameters. These models could distinctively understand the flow dynamics and become a reliable source for predicting local and average *Nu* and S_{gen}. The models are tested against the experimental and the benchmark data, and the results showed how

well ANN models were able to predict the output parameters. The uncertainty analysis showed a 2% error against the benchmark results, and the highest error against the experimental results was obtained at around 1.33%. The coefficient of determination is also used to show the predictive capabilities of the proposed models. Considering all the aspects of predictive models, the proposed models were able to satisfactorily predict the output parameters. Since the results' accuracy was highly important to us, we utilized single models for each output parameter. This way, we were able to achieve higher accuracy in the predictions. Finally, empirical correlations are proposed and a double-factorial optimization of Nu and S_{gen} is presented. The result of double-factorial optimization proved that the best case for both Nu and S_{gen} is when Re is higher than 1600 and the nanoparticle concentration is about 3%. The reason for selecting this value is as the nanoparticle concentration increase, the stability becomes concerning, so the results of 4% and 3% nanofluids differ by 5%. Thus, it is logical to select the more stable case. Also, the Graetz number is used to compare the results of local Nu and S_{gen}. In future research, it is recommended to use other algorithms, such as random forest or support vector machine, to compare the performance of each model and select the best one. Also, other nanofluids could be tested to generalize the effect of nanoparticles. Another recommendation could be replicating the same study for turbulent flows, which has a lot of challenges.

Authors statement

All authors agreed to publish this version of the paper.

Declaration of competing interest

The authors declare that they have no known competing financial interests or personal relationships that could have appeared to influence the work reported in this paper.

Data availability

Data will be made available on request.

Acknowledgments

This work was supported by the King Khalid University, Abha, Saudi Arabia. The authors extend their appreciation to the Deanship of Scientific Research at King Khalid University for funding this work through Larg Groups Project under grant number (R.G.P. 2/43/44).

References

[1] J.C. Maxwell, A Treatise on Electricity and Magnetism, 1, Clarendon press, 1873.
[2] S.U. Choi, J.A. Eastman, Enhancing Thermal Conductivity of Fluids with Nanoparticles (No. ANL/MSD/CP-84938; CONF-951135-29), Argonne National Lab (ANL), Argonne, IL (United States), 1995.
[3] H. Masuda, A. Ebata, K. Teramae, Alteration of thermal conductivity and viscosity of liquid by dispersing ultra-fine particles, Dispersion of Al2O3, SiO2 and TiO2 ultra-fine particles (1993).
[4] B.C. Pak, Y.I. Cho, Hydrodynamic and heat transfer study of dispersed fluids with submicron metallic oxide particles, Experimental Heat Transfer an International Journal 11 (2) (1998) 151–170.
[5] Y. Ding, H. Alias, D. Wen, R.A. Williams, Heat transfer of aqueous suspensions of carbon nanotubes (CNT nanofluids), Int. J. Heat Mass Tran. 49 (1–2) (2006) 240–250.
[6] M. Roodbari, H. Alimoradi, M. Shams, C. Aghanajafi, An experimental investigation of microstructure surface roughness on pool boiling characteristics of TiO2 nanofluid, J. Therm. Anal. Calorimetry 147 (4) (2022) 3283–3298.
[7] H. Alimoradi, M. Shams, N. Ashgriz, Enhancement in the pool boiling heat transfer of copper surface by applying electrophoretic deposited graphene oxide coatings, Int. J. Multiphas. Flow (2022), 104350.
[8] M. Hasheminasab, A. Bozorgnezhad, M. Shams, G. Ahmadi, H. Kanani, Simultaneous investigation of PEMFC performance and water content at different flow rates and relative humidities, in: International Conference on N*anochannels, Microchannels, and Minichannels* 46278, American Society of Mechanical Engineers, 2014, August. V001T07A002.
[9] A. Bozorgnezhad, M. Shams, G. Ahmadi, H. Kanani, M. Hasheminasab, The experimental study of water accumulation in PEMFC cathode channel, in: Fluids Engineering Division *Summer Meeting* 57212, American Society of Mechanical Engineers, 2015, July. V001T22A004.
[10] S. Zaboli, H. Alimoradi, M. Shams, Numerical investigation on improvement in pool boiling heat transfer characteristics using different nanofluid concentrations, J. Therm. Anal. Calorimetry (2022) 1–18.
[11] E. Eskandari, H. Alimoradi, M. Pourbagian, M. Shams, Numerical investigation and deep learning-based prediction of heat transfer characteristics and bubble dynamics of subcooled flow boiling in a vertical tube, Kor. J. Chem. Eng. 39 (12) (2022) 3227–3245.
[12] A.H. Mazandarani, A. Torabian, H.A. Panahi, Removal of codeine phosphate from water and artificial wastewater using sand modified with amine and carboxylic acid groups, Desalination Water Treat. 131 (2018) 261–271.
[13] H. Alimoradi, S. Zaboli, M. Shams, Numerical simulation of surface vibration effects on improvement of pool boiling heat transfer characteristics of nanofluid, Kor. J. Chem. Eng. 39 (1) (2022) 69–85.
[14] Q. Li, Y. Xuan, Convective heat transfer and flow characteristics of Cu-water nanofluid, Sci. China E 45 (4) (2002) 408–416.
[15] M. Sheikholeslami, Efficacy of porous foam on discharging of phase change material with inclusion of hybrid nanomaterial, J. Energy Storage 62 (2023), 106925.
[16] M. Sheikholeslami, Numerical investigation of solar system equipped with innovative turbulator and hybrid nanofluid, Sol. Energy Mater. Sol. Cell. 243 (2022), 111786.
[17] M. Sheikholeslami, Modeling investigation for energy storage system including mixture of paraffin and ZnO nanopowders considering porous media, J. Petrol. Sci. Eng. 219 (2022), 111066.
[18] M. Sheikholeslami, Z. Ebrahimpour, Thermal improvement of linear Fresnel solar system utilizing Al2O3-water nanofluid and multi-way twisted tape, Int. J. Therm. Sci. 176 (2022), 107505.
[19] J.A. Esfahani, P.B. Shahabi, Effect of non-uniform heating on entropy generation for the laminar developing pipe flow of a high Prandtl number fluid, Energy Convers. Manag. 51 (11) (2010) 2087–2097.

[20] A. Noghrehabadi, M.R. Saffarian, R. Pourrajab, M. Ghalambaz, Entropy analysis for nanofluid flow over a stretching sheet in the presence of heat generation/absorption and partial slip, J. Mech. Sci. Technol. 27 (3) (2013) 927–937.
[21] T. Wang, Z. Huang, G. Xi, Entropy generation for mixed convection in a square cavity containing a rotating circular cylinder using a local radial basis function method, Int. J. Heat Mass Tran. 106 (2017) 1063–1073.
[22] Y. Zhou, L. Zhu, J. Yu, Y. Li, Optimization of plate-fin heat exchangers by minimizing specific entropy generation rate, Int. J. Heat Mass Tran. 78 (2014) 942–946.
[23] A. Falahat, M. Shabani, M.R. Saffarian, Entropy generation of pseudo-plastic non-Newtonian nanofluids in circular duct under constant wall temperature, J. Mech. Eng. Technol. 10 (1) (2018) 1–10.
[24] S.A. Abdollahi, P. Jalili, B. Jalili, H. Nourozpour, Y. Safari, P. Pasha, D.D. Ganji, Computer Simulation of Cu: AlOOH/water in a Microchannel Heat Sink Using a Porous Media Technique and Solved by Numerical Analysis AGM and FEM, Theoretical and Applied Mechanics Letters, 2023, 100432.
[25] P. Jalili, H. Narimisa, B. Jalili, D.D. Ganji, Micro-polar nanofluid in the presence of thermophoresis, hall currents, and Brownian motion in a rotating system, Mod. Phys. Lett. B (2023).
[26] P. Jalili, H. Narimisa, B. Jalili, A. Shateri, D.D. Ganji, A novel analytical approach to micro-polar nanofluid thermal analysis in the presence of thermophoresis, Brownian motion and Hall currents, Soft Comput. (2022) 1–13.
[27] P. Jalili, A.A. Azar, B. Jalili, Z. Asadi, D.D. Ganji, Heat transfer analysis in cylindrical polar system with magnetic field: a novel Hybrid Analytical and Numerical Technique, Case Stud. Therm. Eng. 40 (2022), 102524.
[28] B. Jalili, A.D. Ganji, P. Jalili, S.S. Nourazar, D.D. Ganji, Thermal analysis of Williamson fluid flow with Lorentz force on the stretching plate, Case Stud. Therm. Eng. 39 (2022), 102374.
[29] B. Jalili, H. Ghafoori, P. Jalili, Investigation of carbon nanotube (CNT) particles effect on the performance of a refrigeration cycle, Int. J. Mater. Sci. Innov 2 (1) (2014) 8–17.
[30] B. Jalili, S. Sadighi, P. Jalili, D.D. Ganji, Numerical analysis of MHD nanofluid flow and heat transfer in a circular porous medium containing a Cassini oval under the influence of the Lorentz and buoyancy forces, Heat Transfer 51 (7) (2022) 6122–6138.
[31] P. Jalili, K. Kazerani, B. Jalili, D.D. Ganji, Investigation of thermal analysis and pressure drop in non-continuous helical baffle with different helix angles and hybrid nanoparticles, Case Stud. Therm. Eng. 36 (2022), 102209.
[32] B. Jalili, N. Aghaee, P. Jalili, D.D. Ganji, Novel usage of the curved rectangular fin on the heat transfer of a double-pipe heat exchanger with a nanofluid, Case Stud. Therm. Eng. 35 (2022), 102086.
[33] M.H. Esfe, A.A.A. Arani, A.H. Niroumand, W.M. Yan, A. Karimipour, Mixed convection heat transfer from surface-mounted block heat sources in a horizontal channel with nanofluids, Int. J. Heat Mass Tran. 89 (2015) 783–791.
[34] H. Alimoradi, M. Soltani, P. Shahali, F. Moradi Kashkooli, R. Larizadeh, K. Raahemifar, M. Adibi, B. Ghasemi, Experimental investigation on improvement of wet cooling tower efficiency with diverse packing compaction using ANN-PSO algorithm, Energies 14 (1) (2020) 167.
[35] G. Hetsroni, R. Rozenblit, Heat transfer to a liquid—solid mixture in a flume, Int. J. Multiphas. Flow 20 (4) (1994) 671–689.
[36] A.H. Altun, H. Nacak, E. Canli, Effects of trapezoidal and twisted trapezoidal tapes on turbulent heat transfer in tubes, Appl. Therm. Eng. 211 (2022), 118386.
[37] Ö. Özenbiner, A. Yurddaş, Numerical analysis of heat transfer of a nanofluid counter-flow heat exchanger, Int. Commun. Heat Mass Tran. 137 (2022), 106306.
[38] S. Sivasankaran, M. Bhuvaneswari, Numerical study on influence of water based hybrid nanofluid and porous media on heat transfer and pressure loss, Case Stud. Therm. Eng. 34 (2022), 102022.
[39] H. Alimoradi, M. Shams, N. Ashgriz, Bubble behavior and nucleation site density in subcooled flow boiling using a novel method for simulating the microstructure of surface roughness, Kor. J. Chem. Eng. 39 (11) (2022) 2945–2958.
[40] S.U.S. Choi, Z.G. Zhang, W. Yu, F.E. Lockwood, E.A. Grulke, Anomalous thermal conductivity enhancement in nanotube suspensions, Appl. Phys. Lett. 79 (14) (2001) 2252–2254.
[41] Y. Xuan, W. Roetzel, Conceptions for heat transfer correlation of nanofluids, Int. J. Heat Mass Tran. 43 (19) (2000) 3701–3707.
[42] K. Khanafer, K. Vafai, M. Lightstone, Buoyancy-driven heat transfer enhancement in a two-dimensional enclosure utilizing nanofluids, Int. J. Heat Mass Tran. 46 (19) (2003) 3639–3653.
[43] S.K. Das, S.U. Choi, H.E. Patel, Heat transfer in nanofluids—a review, Heat Tran. Eng. 27 (10) (2006) 3–19.
[44] R.B. Mansour, N. Galanis, C.T. Nguyen, Effect of uncertainties in physical properties on forced convection heat transfer with nanofluids, Appl. Therm. Eng. 27 (1) (2007) 240–249.
[45] P.K. Namburu, D.K. Das, K.M. Tanguturi, R.S. Vajjha, Numerical study of turbulent flow and heat transfer characteristics of nanofluids considering variable properties, Int. J. Therm. Sci. 48 (2) (2009) 290–302.
[46] S.E.B. Maïga, C.T. Nguyen, N. Galanis, G. Roy, Heat transfer behaviours of nanofluids in a uniformly heated tube, Superlattice. Microst. 35 (3–6) (2004) 543–557.
[47] A. Behzadmehr, M. Saffar-Avval, N. Galanis, Prediction of turbulent forced convection of a nanofluid in a tube with uniform heat flux using a two phase approach, Int. J. Heat Fluid Flow 28 (2) (2007) 211–219.
[48] E. Heidari, M.A. Sobati, S. Movahedirad, Accurate prediction of nanofluid viscosity using a multilayer perceptron artificial neural network (MLP-ANN), Chemometr. Intell. Lab. Syst. 155 (2016) 73–85.
[49] M. Hemmat Esfe, S. Saedodin, M. Bahiraei, D. Toghraie, O. Mahian, S. Wongwises, Thermal conductivity modeling of MgO/EG nanofluids using experimental data and artificial neural network, J. Therm. Anal. Calorimetry 118 (1) (2014) 287–294.
[50] H. Alimoradi, E. Eskandari, M. Pourbagian, M. Shams, A parametric study of subcooled flow boiling of Al2O3/water nanofluid using numerical simulation and artificial neural networks, Nanoscale Microscale Thermophys. Eng. (2022) 1–31.
[51] H. Alimoradi, M. Shams, Optimization of subcooled flow boiling in a vertical pipe by using artificial neural network and multi objective genetic algorithm, Appl. Therm. Eng. 111 (2017) 1039–1051.
[52] A.E. Jery, P. Satishkumar, M. Abdul Jaleel Maktoof, M. Suplata, B. Dudic, V. Spalevic, Sustainable heat transfer management: modeling of entropy generation minimization and Nusselt number development in internal flows with various shapes of cross-sections using water and Al2O3/water nanofluid, Water 15 (2023) 89, https://doi.org/10.3390/w15010089.
[53] L.S. Sundar, M.T. Naik, K.V. Sharma, M.K. Singh, T.C.S. Reddy, Experimental investigation of forced convection heat transfer and friction factor in a tube with Fe3O4 magnetic nanofluid, Exp. Therm. Fluid Sci. 37 (2012) 65–71.
[54] A. Moghadassi, F. Parvizian, S. Hosseini, A new approach based on artificial neural networks for prediction of high pressure vapor-liquid equilibrium, Australian Journal of Basic and Applied Sciences 3 (3) (2009) 1851–1862.
[55] R. Collobert, S. Bengio, Links between perceptrons, MLPs and SVMs, in: Proceedings of the Twenty-First International Conference on Machine Learning, 2004, July, p. 23.
[56] D. Svozil, V. Kvasnicka, J. Pospichal, Introduction to multilayer feed-forward neural networks, Chemometr. Intell. Lab. Syst. 39 (1) (1997) 43–62.